Transport through composite membrane, part 1: Is there an optimal support membrane?

Guy Z. Ramon [1], Mavis C.Y. Wong, Eric M.V. Hoek *

Department of Civil & Environmental Engineering & California NanoSystems Institute, University of California, 5732-G Boelter Hall, P.O. Box 951593, Los Angeles, CA 90095-1593, USA

ARTICLE INFO

ABSTRACT

The effects of the support membrane pore size and porosity on diffusive transport through composite membranes have been investigated theoretically. Both 3D and 2D models were developed to mechanistically describe the relationship between support membrane pore structure, support material permeability, coating film thickness and the resulting composite membrane permeability; in addition, an analytical model was developed as an approximate, but more convenient approach for assessing trends of composite membrane transport. Model results suggest the choice of support is increasingly important as thin film permeability increases (i.e., less dense or thinner). For fixed coating film permeability, changes to support membrane pore structure create practically important changes to observed water flux and salt rejection by nanofiltration, brackish water reverse osmosis (RO), and seawater RO membranes. The diffusivity of the permeating species in the microporous phase of the support material may also contribute to the overall permeability of the composite membrane. Finally, a systematic numerical study suggests, for the first time, that the local permeate water flux through composite membranes is dictated by support membrane pore morphology, creating localized high flux "hot spots" with potentially high fouling and scaling propensity.

© 2012 Elsevier B.V. All rights reserved.

1. Introduction

Composite membrane materials comprised of a thin coating film formed over a porous support membrane are the basis for state-of-the-art membranes now used for gas separations [1], pervaporation [2], and osmotic separations (NF/RO/FO) [3]. The composite membrane approach allows independent tailoring and optimization of the support membrane [4,5] and the coating film [6,7,8]. Until recently, except in the case of FO membranes [9], limited information exists in the open literature about the impacts that support membrane physical–chemical properties have on composite membrane formation and resulting performance. Such potential effects may be separated into two categories: (1) the support membrane's surface chemistry and pore structure may influence the thickness, roughness, and cross-linked structure of films (especially those formed by interfacial polymerization) and (2) for a given coating film structure, the pore size and porosity of the underlying support may contribute significantly to diffusive transport through the composite structure.

The former effect appears to have been first described only recently (in the open literature) by Ghosh and Hoek [10], while the latter effect was first described by Lonsdale et al. [11] over 4 decades ago. Here, we focus on the latter. The basic concept is that the support membrane hinders the transport of diffusing species at its interface with the coating film due to partial blockage by the solid fraction, while the liquid phase within the pores allows mass transfer to proceed at a significantly higher rate. These preferential sites for transport through the bottom of the thin coating film result in a lateral transport through the film proportional to the characteristic support membrane pore spacing. In their paper, Lonsdale and co-workers experimentally demonstrate differences in water permeability of cellulosic composite membranes by tailoring the pore structure of the support membrane. A numerical solution of a 2D, axisymmetric geometry was also presented, illustrating the general trends that emerge when the support pore size and porosity is varied. Despite the fact that Lonsdale et al.'s seminal publication has only been cited 12 times (per *ISI Web of Knowledge*, as of January 11, 2012), the role of the support membrane in composite membrane separation performance is well known in the membrane industry and to anyone experienced at fabricating composite membranes.

The RO-membrane specific problem described by Lonsdale et al. was later examined in a more general way by Davis and Ethier [12] who constructed a series solution of the Laplace equation, which describes the concentration field in the thin film, providing a semi-analytical solution to describe diffusive transport through a dense film formed on top of a porous substrate. Fane and co-workers [13] describe fouling behavior of ultrafiltration (UF) membranes using

* Corresponding author. Tel.: +1 310 206 3735; fax: +1 310 206 2222.
  E-mail address: emvhoek@ucla.edu (E.M.V. Hoek).
[1] Present address: Department of Mechanical and Aerospace Engineering, Princeton University, Princeton, NJ, 08544, USA.

this concept, analogizing composite membrane transport to the relatively dense protein gel layer formed over sparingly porous UF membranes. Ethier and Kamm [14] numerically solved the case of hemispherical deposits at the vicinity of a pore opening when considering the permeability of a cake layer deposited over a porous membrane. Some similar work has also been published in the context of composite membranes used for gas separation [15,16]; in these, the effect of pore transport also becomes important due to additional separation of gas species through Knudsen diffusion. Despite these publications, to the best of our knowledge, no other studies have been published that mechanistically examined the role of support membrane pore morphology on transport through composite membranes.

Herein, the problem of transport through a composite membrane is re-visited theoretically, with the goal of further elucidating the practical implications for NF and RO membranes as influenced by the choice of support membrane; specifically, we probe possible avenues for exploiting the support pore structure and material transport properties for minimizing the detrimental impact of the support on the overall permeability of the composite. To this end, we employ both 2D and 3D numerical models and an approximate analytical expression to explore the impacts of support membrane pore size and porosity along with coating film thickness on (a) the apparent permeability of composite membranes, (b) the observed flux and solute rejection assuming representative thin film properties of modern NF/RO membranes, and (c) the local distribution of flux through composite membranes.

2. Theory

The purpose of the developed model was to assess, quantitatively, the impact of the support geometrical features, namely pore size and porosity, on the characteristics of the water and salt flux through the selective film; further, the effect of the support material permeability has also been examined. The geometric configurations used in the computations are shown in Fig. 1a and b for the 2D axisymmetric case and in Fig. 1c and d for the 3D case. For simplicity, in the 3D model surface porosity at the support–film interface was assumed ordered in a square-array as depicted schematically in Fig. 1c, allowing the computational model to be defined on a periodic cell. A unit cell used for the 3D computation is shown in Fig. 1d, where the inherent symmetry of the system has been used to reduce the size of the domain, and hence, the computational requirements. This geometry, while still an obvious idealization, nevertheless constitutes a more realistic depiction and a possible improvement over the 2D, axisymmetric model considered in previous publications [11,12], (see Fig. 1c). This is due to the fact that the 3D cell accounts for regions of the film, which are not symmetrically distributed about each pore—these are neglected in the axis-symmetric cell. Moreover, it is a simple matter to observe that of all possible periodic arrays in 3D, the square array will result in the largest added area; closer packed periodic arrays will invariably have smaller deviations from the axis-symmetric cell. We therefore expect that the chosen array is illustrative of the greatest deviation expected between a 3D and 2D description, and serves as an indication of the trade-off between computational requirements and quantitative accuracy.

2.1. Numerical model

In the following model, it is assumed that transport through the film is diffusive, and is therefore dictated by gradients in a chemical potential of the diffusing species, which may be water or salt. For conciseness of representation, the chemical potential is replaced here with a concentration, which is scaled such that it is unity at the interface between the coating film and the feed stream; the support
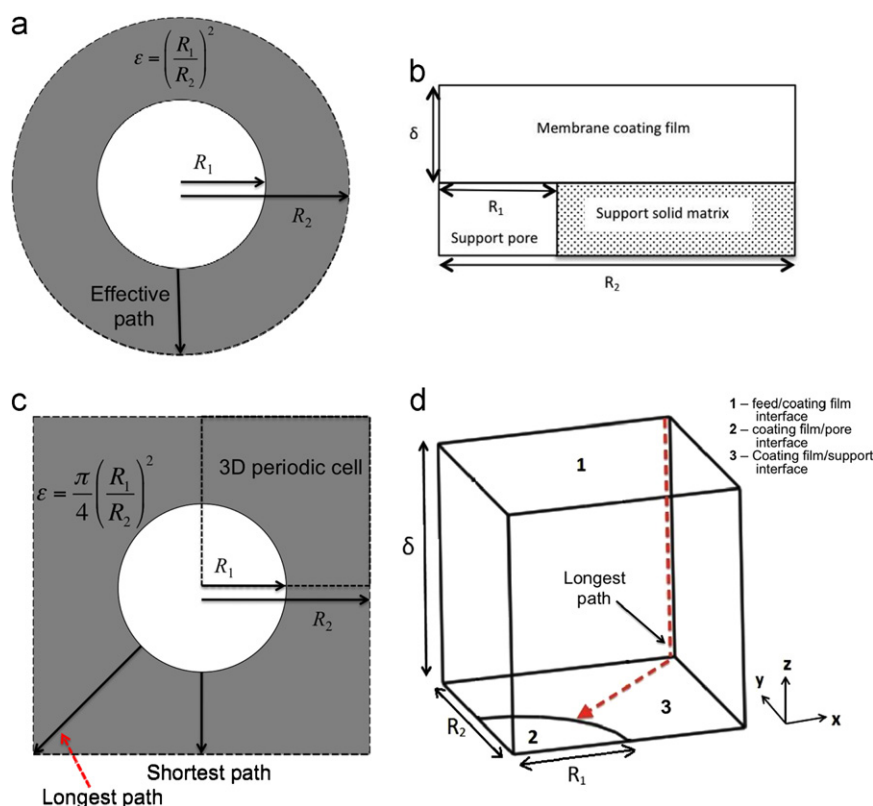

Fig. 1. Schematic drawings illustrating the geometry used for the model calculations. (a) 'Top' view of an axis-symmetric unit cell. (b) A side view of the 2D cell. (c) 'Top' view of a unit-cell in a square array. (d) The slice used for the 3D numerical model.

pore is assumed to be filled with water, and so transport within the pore is convective and assumed to dominate over the diffusion within the film. The appropriate boundary condition under this assumption is that of a perfect sink, or zero concentration. Physically, this means that a diffusing species reaching the interface is instantaneously removed. We note, however, that in a strict sense for any combination of boundary concentrations in the feed and permeate (pore) the concentration may be scaled such that it will vary between 0 and 1; this is convenient since we are interested in any permeating species (be it water or solute) and so it should not be considered as indicative of full rejection.

The steady-state concentration field within the film is governed by the Laplace equation:

$$\frac{\partial^2 C}{\partial X^2} + \frac{\partial^2 C}{\partial Y^2} + \frac{\partial^2 C}{\partial Z^2} = 0, \tag{1}$$

where C is the scaled concentration, and X, Y, Z are the Cartesian coordinates, scaled by the pore radius, R_1. Note that to facilitate the comparison with 2D calculations (both our own as well as published results) lengths will be scaled by the pore-to-pore spacing, R_2, while for all other calculations the pore radius, R_1, is chosen as the characteristic length scale.

The boundary conditions are imposed, as follows:

At the film/feed solution interface (marked with the number 1 in Fig. 1d)

$$C = 1 \tag{2a}$$

At the film/pore interface (marked as number 2 in Fig. 1d)

$$C = 0 \tag{2b}$$

At the interface between the film and support material, the part of the bottom X–Y plane occupied by the support material (marked as number 3 in Fig. 1d), continuity of the flux requires:

$$D_f \frac{\partial C_f}{\partial Z} = D_s \frac{\partial C_s}{\partial Z}, \tag{2c}$$

where D is the diffusion coefficient in the diffusing species within either the film or the support, here distinguished by the subscripts f and s, respectively. In all the performed 3D simulations it is assumed that the support material is, for all practical considerations, impermeable; hence, the diffusivity of the support is taken as zero resulting in a no-flux condition. This condition has been relaxed for some of the 2D simulations in order to assess the possible impact of a permeable support material. Since the support thickness is several orders of magnitudes greater than the film thickness, it may be considered as an infinitely extended region; in the numerical model, this was implemented by requiring that the thickness of the support be large enough so that it does not influence the resulting concentration field. A no-flux condition is imposed on the remaining boundaries, due to symmetry considerations. We note that these boundary conditions are identical to those employed in previous studies [11,12], save the flux continuity condition expressed by Eq. (2c), which extends these previous models to consider the possibility of a permeable support material. Eq. (1), along with the boundary conditions, was solved numerically employing a commercial finite-element package (Comsol Multi-Physics, version 3.5a). An adaptive mesh function was used to ensure adequate refining of the mesh in the regions where the boundary condition transitions from a constant concentration to a no-flux condition. This has previously been shown to cause significant errors in the computation [12]; therefore, refinement was continued until the calculated solution became mesh-independent.

2.2. Analytical scaling-law model

In a simplified, 1D depiction of the diffusive water transport through the membrane film, the steady-state flux may be written as

$$J = D \frac{\Delta C}{\delta} \tag{3}$$

where D is the diffusion coefficient for water within the membrane, δ is the membrane film thickness and ΔC is the concentration difference across the film (scaled such that it is unity, in our case). Now, Eq. (3) describes the water flow (or solute flux), per unit area of membrane, for the 'ideal' case where no constraint is imposed by the support. As first pointed out by Lonsdale et al. [11], when the support is accounted for the water transport will be reduced since part of the membrane film is effectively blocked. Under such conditions, however, it may still be possible to define an 'effective' thickness, δ_{eff}, accounting for the altered diffusion path of the water. Fig. 1c and d may be used to illustrate this point through simple geometric considerations; the path traversed by water diffusing through the film is influenced by the initial location, on the membrane–feed interface, with respect to the support membrane pore entrance through which water may diffuse out of the film, and it also depends on the size of the pore.

Taking the ratio of the 'real' and 'ideal' fluxes, for identical concentration gradient and diffusivity results in the following expression:

$$\frac{J_{real}}{J_{ideal}} = \frac{\delta}{\delta_{eff}} = \frac{P_{real}}{P_{ideal}}, \tag{4}$$

where P is the membrane permeability. Eq. (4) illustrates that the 'real' flux will be smaller than the 'ideal' one by a factor, which is proportional to the inverse of the 'effective' diffusion path-length. This inverse 'effective' path-length, if scaled by R_2, is identical to the 'geometric factor' as defined in previous studies [11,12].

Next, we approximate the 'effective' path-length by assuming a mixing-rule by which the occurrence of the shortest and longest possible paths for diffusion will be in proportion to the porosity and solidosity, respectively, or

$$\delta_{eff} = \varepsilon \delta_S + (1-\varepsilon)\delta_L \tag{5}$$

with subscripts S and L denoting short and long, respectively. The shortest path is, simply, the film thickness, hence $\delta_S = \delta$. Using the simplified geometry of the square-array, the longest path is taken as that between the farthest point on the membrane–feed interface, to the pore boundary:

$$\delta_L = \delta + (\sqrt{2}R_2 - R_1) \tag{6}$$

Using the definition of the surface porosity in a square-array, given as $\varepsilon = (\pi/4)(R_1/R_2)^2$, we eliminate R_2 from Eq. (6) to obtain

$$\delta_{eff} = \varepsilon \delta + (1-\varepsilon)\left(\delta + \sqrt{\frac{\pi R_1^2}{\varepsilon}} - R_1\right) \tag{7}$$

This simple expression shows the dependence of the 'effective' diffusion path-length (or effective film thickness) on the porosity and pore-size of the support membrane. The applicability of this expression in predicting the general trends found through numerical simulations will be presented and discussed later.

3. Results and discussion

3.1. Numerical simulations

We begin by examining the characteristics of the 3D concentration field (Fig. 2) for two cases, defined by the value of the scaled film thickness, $H = \delta/R_1$, and the surface porosity of the support, ε. Both cases have been calculated with a scaled film thickness of $H = 2$, but with differing porosities of $\varepsilon = 0.1$ (Fig. 2a and b)
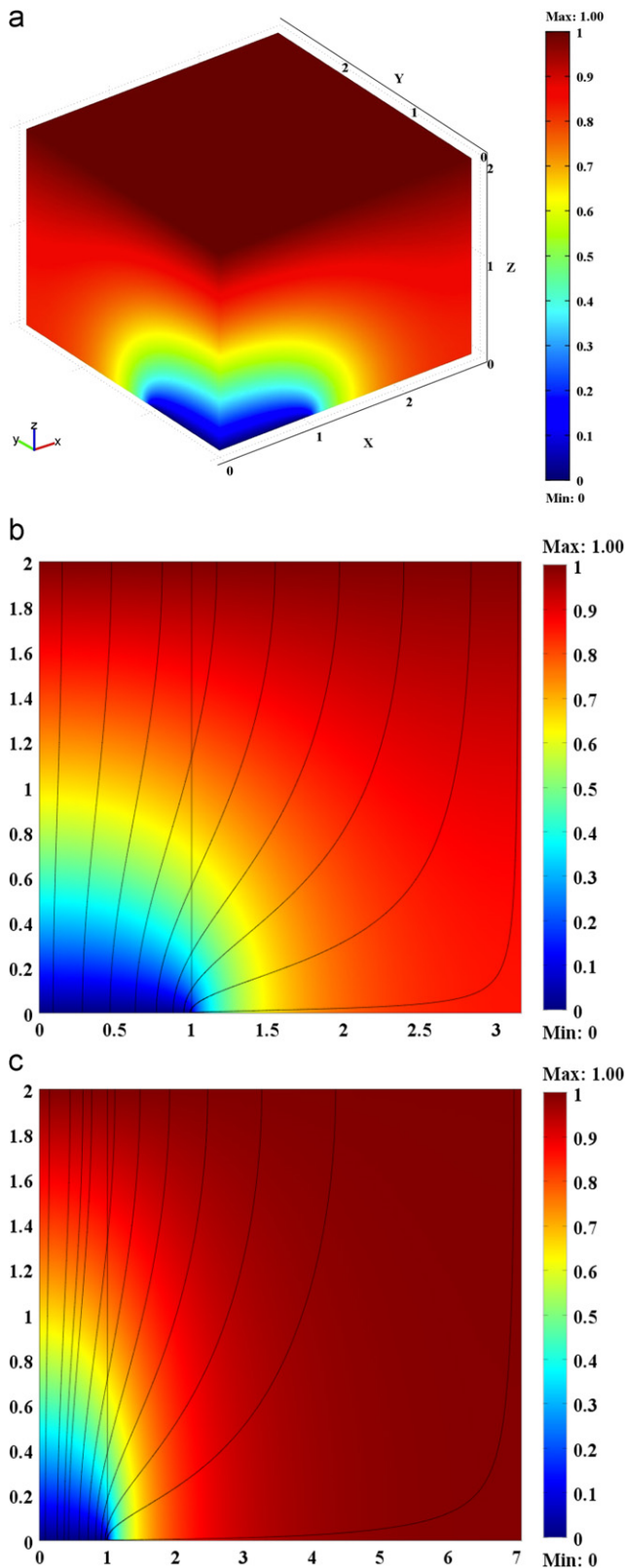
Fig. 3. The scaled permeability, P_{real}/P_{ideal}, as a function of the 2D porosity, R_1/R_2, for different values of the scaled thickness, δ/R_2, calculated for 2D (solid) and 3D (dashed). The dots are calculated based on the numerical results, tabulated in Davis and Ethier [12]. Note that the different scaling used here (with respect to R_2) is for comparison with the literature.

opening; as the porosity increases this becomes significantly less pronounced and the entire film section is subject to significant concentration variations. Note that a porosity of 0.1 may be very high for typical polysulfone support membranes used for RO composites; nevertheless, it serves as an illustration of the range of porosity for which the diffusion into the pore.

Also shown in these figures are 'streamlines' which indicate some representative diffusive paths through the film for each case. The effect of a reduced porosity is quite apparent; with the reduction of porosity the section of the membrane which is 'active' in transporting the diffusing species diminishes and becomes more and more restricted to the pore region (marked as a vertical line, at a scaled distance of 1 from the pore center). When either the thickness or porosity are substantially increased, the flux distribution within the membrane becomes more even and the dependence on the porosity becomes smaller. The asymptotic dependence of an extremely 'thin' film would approach a pure porosity dependence, as already pointed out intuitively by Lonsdale et al. [11] and later confirmed rigorously by Davis and Ethier [12].

The scaled permeability, P_{real}/P_{ideal}, was calculated over a range of porosities and film thicknesses. The simulation results plotted in Fig. 3 allow comparison of the 3D numerical model calculations with the 2D numerical axisymmetric geometry, and with published numerical calculations made for the same 2D geometry [12]. Note that the scaling used in these calculations is different (made with respect to R_2) to facilitate the comparison with published values. As may be seen, there is a small variation between the 2D and 3D results with the 2D calculations over-predicting the permeability; this may be expected since the 2D geometry has an inherently higher porosity. The tabulated 2D results of Davis and Ethier [12] match almost perfectly with our numerical 2D results, deviating slightly for 'thin' membranes, which is beyond the limits of validity for the tabulated data [12]. Overall, the deviation between 2D and 3D (generally < 10%) may not be large enough to justify the considerably greater computational effort in producing 3D numerical simulation results.

3.2. Comparison of analytical and numerical calculations

Next, the numerical calculations are briefly compared with our proposed 'scaling-law' analytical expression given by Eq. (7), as may be seen in Fig. 4. It is important to note that Eq. (7) relies on a simplified, intuitive depiction of the physical problem and so it is not expected to produce quantitatively accurate results; rather, its utility is in producing easy to compute, qualitatively accurate trends. As such, it is in reasonable quantitative agreement with numerical calculations. When the support porosity is low, the analytical approximation significantly over-predicts the value of the scaled permeability, compared with the numerical calculations, and this is particularly noticeable for 'thick' films (relative to the pore radius, which is used to scale the thickness). As porosity increases, the analytical model under-predicts the effective film permeability, particularly for 'thin' films. In light of the insight gained from the numerical calculations shown in the previous section, this may be explained as follows. At low porosities, the pore area available at the film/support interface is the primary determinant for the flux through the film, since the rest of the film/support interface is non-permeable. Hence, the mixing with a long path length is, in fact, redundant and causes the predicted flux to be higher than expected. On the other hand, for high porosities, the restriction imposed by the pores becomes less important, streamlines are seen to become straighter and there is a 'pinching' effect at the pore entrance, whereby streamlines originating above the pore location are pushed into an inner location;

Fig. 2. Representative plot of the numerical solution, for a scaled film thickness, $H = \delta/R_1 = 2$. (a) The 3D concentration field. (b) Diffusive 'flow' paths, obtained from the numerical solution, shown along the X–Z plane for a support surface porosity $\varepsilon = 0.1$. (c) Same as (b), with $\varepsilon = 0.01$.

and $\varepsilon = 0.02$ (Fig. 2c). This choice was made to reflect the impact of support membrane surface porosity on the concentration field, and hence, on the flux through the film. As may be seen, a low porosity clearly confines the flux (which may be visualized from the concentration gradients) to the vicinity of the pore
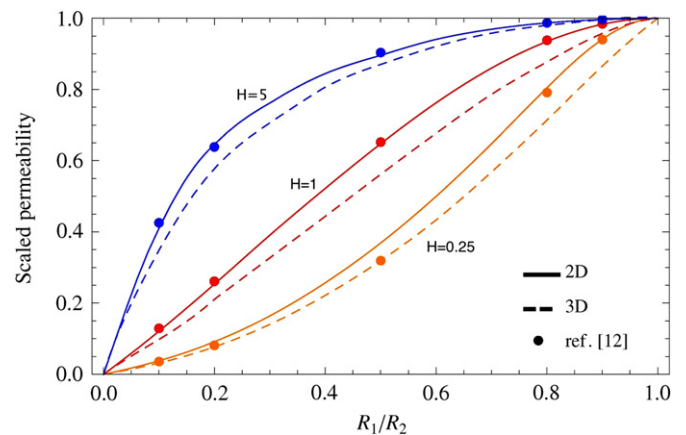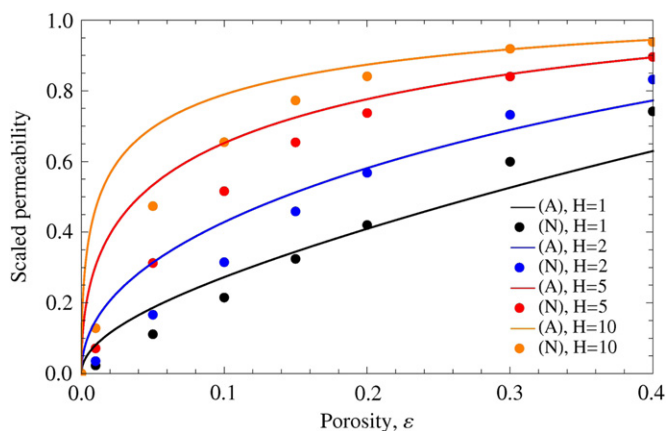
Fig. 4. The scaled permeability, P_{real}/P_{ideal}, as a function of the porosity, for different values of the scaled thickness, $H = \delta/R_1$. Solid lines (A) are calculations made using the analytical scaling-law given by Eq. (7), while the dotted values (N) were obtained from the 3D numerical solution.

this results in an 'effective' pore size which is larger than the nominal one. This physical behavior cannot be captured by the simple mixing-rule employed in deriving Eq. (7), though its utility is nonetheless apparent. Over the range of porosities $\varepsilon = 0.05$–0.4 (shown in Fig. 4), the average deviation between the numerical and analytical calculations is ~15% for $H = 1$ and ~12% for $H = 10$. However, at the low porosities found in practice (~0.01–0.05), the mixing-rule approximation deviates much more substantially, over-predicting the scaled permeability up to a factor of 4 in the case of relatively thick films ($H > 10$). Therefore, the analytical expression is a useful, but coarse tool for assessing general trends and should be considered semi-quantitative at best. For extremely low film thicknesses, scaling the permeability directly with the porosity provides a better approximation; at this point, transport through the membrane is completely dictated by the pore openings at the interface between the support and coating film.

3.3. General trends for flux and rejection

Variations in support membrane porosity and pore size produce opposing trends for observed rejection and flux (the latter plotted as flux divided by applied pressure in Fig. 5); identical coating film A and B values were used in these simulations (see Table A1). For example, if one seeks to maximize rejection, the choice of support should be one with relatively low porosity and large pores; conversely, for maximizing flux one should use a more porous support with smaller pores. Moreover, considering operating conditions to be equal and varying only the support porosity and pore-size, the flux and rejection are altered to a degree that is dictated by the intrinsic transport properties of the coating film; that means intrinsically more permeable coating films (i.e., NF) are more greatly affected by changes in support membrane pore structure.

Rejection and specific flux calculations were made using parameters representative of seawater RO, brackish water RO, and freshwater NF membranes (see the appendix for details of the calculation and parameters used). While the trends in rejection clearly follow the same general trend observed for permeability, there are striking differences in the magnitudes of the variations. For the seawater RO membrane, observed rejection varies between ~99.4% and ~99.8% (Fig. 5a and b), while for the NF membrane the rejection ranged from ~80% to ~90% (Fig. 5e and f). Brackish water RO membrane rejection varied to an intermediate extent (Fig. 5c and d). For all three membranes, the flux ranges from its maximal value at the highest porosities and smallest pore sizes, towards zero flux for the lowest porosities and largest pore sizes.

3.4. Flux distribution over the coating film

Considering multiple repeating units of the 2D geometry depicted in Fig. 1b concurrently, a representative membrane segment is generated (see Fig. 6a). Calculations have been made of the flux at the coating film-feed interface for different film thicknesses and two representative porosities, assuming that the support material is impermeable. As may be seen, a distribution in flux values emerges around the support membrane pores and this distribution is highly sensitive to the thickness of the coating film (see Fig. 6b and c). In general, the flux distribution follows the periodicity of the pore distribution. As the film becomes thinner, the scaled flux distribution becomes sharper (here, the flux is scaled against the average flux determined by integrating across the entire film). For a

relatively high porosity ($\varepsilon = 0.05$, see Fig. 6b) and coating film thickness $H = 5$, the local flux ranges from virtually zero between pores to more than ~3.5× the average flux (the highest fluxes are observed directly above the pores). As coating film thickness increases, this flux distribution dampens out; for a membrane 30 times thicker than the support membrane pore radius, there is virtually no variation in the flux. For a lower porosity ($\varepsilon = 0.005$), potentially more representative of practical RO membrane materials, the variation is even sharper—the flux over pore locations is ~9× greater than the surface-averaged flux when the membrane thickness to pore radius ratio is $H = 5$, and even for a thick membrane, with $H = 50$ the flux distribution does not completely flatten out, but still showed a ~15% variation between regions over a pore and the average flux.

The results discussed above suggest that for low porosity support membranes, flux variations may be quite pronounced even for relatively thick coating films. As a representative example, consider an RO membrane with a film thickness of ~100 nm over a support with a pore size of ~5 nm and a porosity of ~0.5%. According to the numerical simulations, for such a membrane with $H = 20$, the flux over the membrane will vary from up to ~2 times to less than half the area average flux, suggesting the possible existence of both 'hot spots' and 'dead zones' with respect to local permeation. This may have important practical implications for early stages of RO membrane fouling and scaling. A locally high flux will promote locally higher concentration polarization and particle deposition rates—possibly offering favorable sites for initiation of mineral scaling or colloidal fouling. In addition to differences in surface roughness or surface chemistry, it seems the historic drive towards forming ultra-thin coating films over mechanically robust supports (the latter achieved using sparingly porous supports) may create local 'hot spots' of very high flux. These hot spots may offer another explanation for the inherently higher fouling propensity of polyamide composite RO membranes relative to cellulosic RO membranes, which have relatively thick skin layers (microns versus nanometers), and hence, virtually uniform permeate flux equal to the surface-averaged value.

3.5. Effect of a permeable support material

In our previous calculations, the support solid phase was treated as an impermeable material; this corresponds to previous published results [11,12]. State-of-the-art composite RO and NF membranes have supports fabricated out of polysulfone or polyethersulfone, a hydrophobic polymer with relatively poor water transport properties. However, we question how reasonable is the assumption of zero permeability of water and salt through the "solid phase" of the support membrane; in fact, this material is microporous and has been used to produce gas separation membranes with no meso-scale or macro-scale surface pores.

Here, we present simulations in which this assumption has been relaxed—the support solid phase has been added to the model as a domain with an assigned diffusion coefficient, providing an additional path for diffusion. For convenience, the diffusivity in the support material is scaled against the diffusivity in the film and so will be referred to as a "relative diffusivity." As shown in previous sections, the support solid phase will, in all cases, reduce the overall permeability of the composite, compared with that of the isolated coating film. However, our simulations indicate that a substantial increase of the composite performance is possible if the support is fabricated out of a material with permeability comparable to that of the coating film. As may be seen in Fig. 7, if a support membrane is fabricated from a material in which the permeant diffusivity is equal to that in the coating film (i.e., relative diffusivity equal to 1), then the overall permeability of the composite may be improved several-fold, particularly for the case of a thin coating film over a low porosity support. If the support diffusivity is further increased, the support's hindrance diminishes and will eventually vanish; this is most noticeable for a thicker coating film, where the impact of the support is intrinsically lower. From a materials standpoint, this offers interesting possibilities; obviously, if the support is made of the same material as the coating film (this is an inherent feature of integrally-skinned, phase-inversion membranes), then its diffusivity will be at least equal to or greater than that of the selective skin. The diffusivity of the support material may be made greater than that of the coating film if it is fabricated with a highly microporous substructure at the interface between the coating film and the support (with 'pore' dimensions on the order of 1–2 nm).

An additional positive feature of a permeable support material is its capacity for dampening the flux distribution by providing additional pathways for diffusion. This may be seen in Fig. 8. A representative simulated segment illustrates the diffusion streamlines (Fig. 8a), which offer a visually intuitive understanding of the increased permeability of the composite; the fluid-filled pore still offers the fastest route for transport, but now has a higher available surface area connected with the solid phase through which the slower diffusive transport occurs. The resulting dampened flux distribution is shown in Fig. 8b, calculated for a composite membrane comprised of a film with $H = 10$ and a porosity of 0.01. If the support material is made to be equally permeable as the coating film, the flux distribution is dampened such that the highest local flux is greater by only ~50% compared with the average flux (as opposed to a 200% variation when the support was taken to be impermeable).
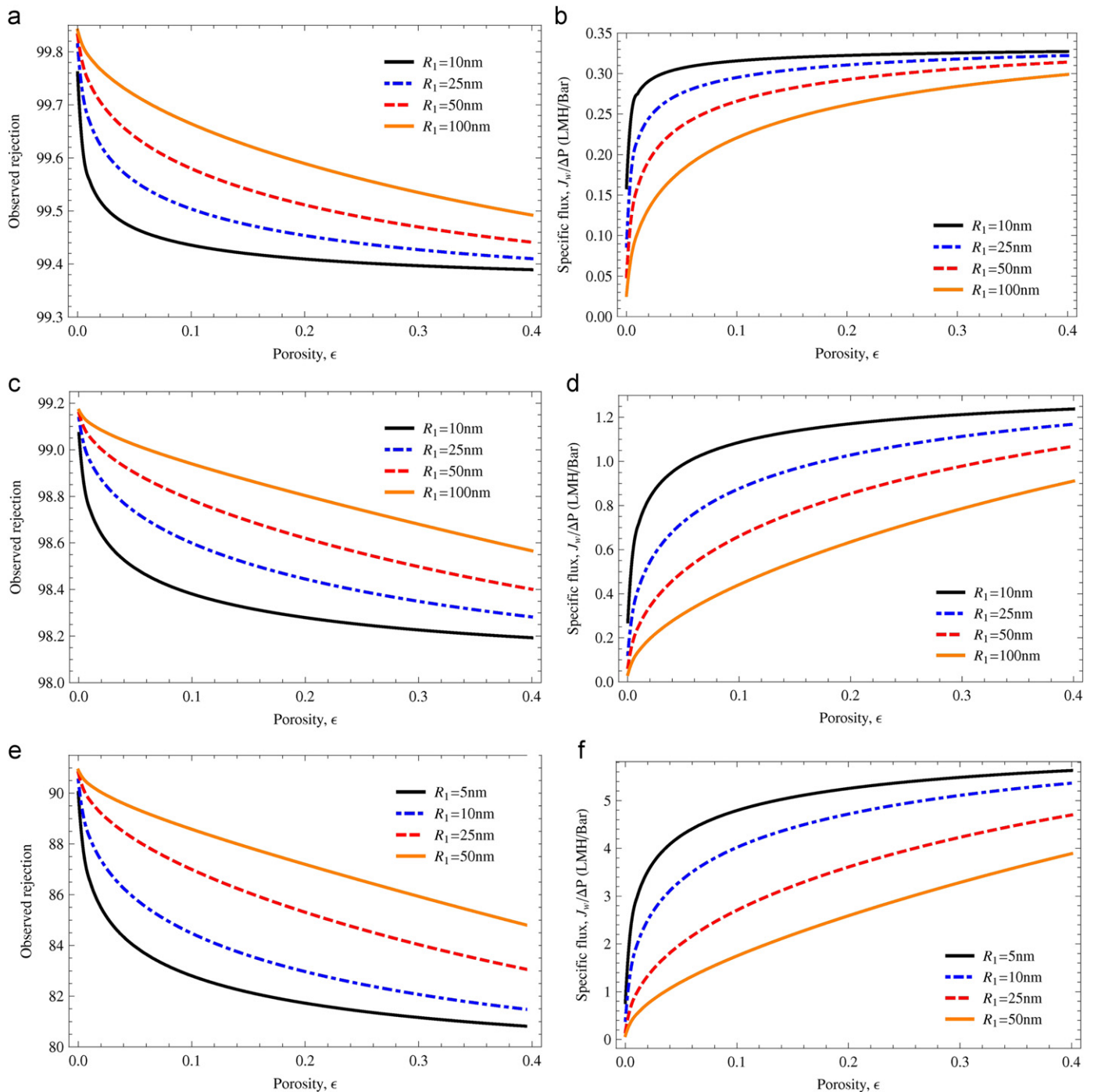
Fig. 5. The observed rejection and specific flux, $J_W/\Delta P$, as a function of the support membrane porosity and pore size. Calculations made using transport coefficients characteristic of (a, b) Seawater RO (c, d) Brackish water RO (e, f) NF. See Table A1 for the parameter values used in the calculations. Note: specific flux is shown in units of L/(m² h) per bar. 1 LMH/bar = 0.04 GFD/psi.

4. Concluding remarks

Modeling results reported herein confirmed previous reports that the permeability of composite RO/NF membranes strongly depends on the skin layer pore structure of the support membrane on which the coating film was formed. Moreover, the presented results suggest it is possible to fine-tune the flux and rejection properties of a composite membrane by varying support membrane skin layer porosity and pore size independent of the properties of the coating film. As a practical point,

NF membrane performance appears much more sensitive to support membrane pore structure than RO membranes. An important extension to previous models, incorporated in our simulations, accounts for diffusion through the microporosity of the support material and illustrates that a dramatic improvement in composite permeability is theoretically possible if transport through the support material proceeds at a rate comparable with that in the coating film. Finally, numerical simulations suggest the existence of a water flux distribution over the surface of a composite membrane—the magnitude of
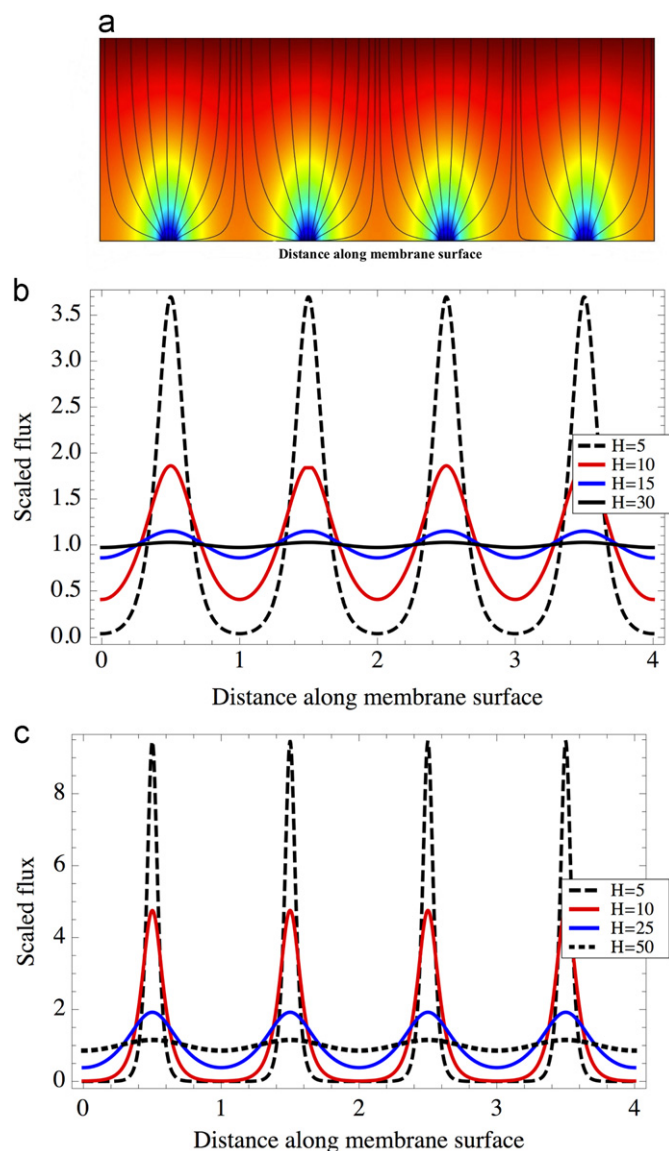
Fig. 6. The effect of support membrane pores on the flux distribution over the composite membrane's selective film. (a) Concentration field (note color coding varies from red to blue, denoting high and low concentration, respectively) and diffusive streamlines in a 4-unit representative membrane, shown for a porosity $\varepsilon = 0.05$ and scaled thickness $H = \delta/R_1 = 10$. (b) The flux, scaled by the average flux through the film, shown for a porosity, $\varepsilon = 0.05$, for various values of the scaled thickness, $H = \delta/R_1$. (c) The scaled flux shown for a porosity, $\varepsilon = 0.005$, for various values of the scaled thickness, $H = \delta/R_1$ (For interpretation of the references to color in this figure caption, the reader is referred to the web version of this article.).

flux maxima and minima governed by support membrane pore structure and coating film thickness. This uneven flux distribution may be dampened substantially by increasing the permeability of the microporous phase of the support membrane. With very thin films and relatively non-permeable support materials, such as those now commonly employed for polysulfone–polyamide composite NF and RO membranes, this inherent variation of flux over the membrane could create local hot spots that contribute to initial stages of membrane fouling and scaling.
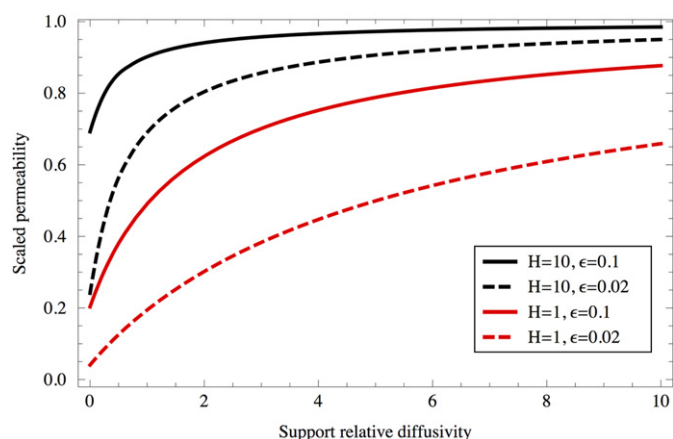
Acknowledgments

Fig. 7. Effect of a permeable support material, shown as the relative diffusivity D_S/D_f, on the overall, scaled permeability of the composite membrane. Calculations made for various support porosities and scaled thicknesses, $H = \delta/R_1$. Equal diffusivity of solutes within the film and support material results in a relative diffusivity of unity.
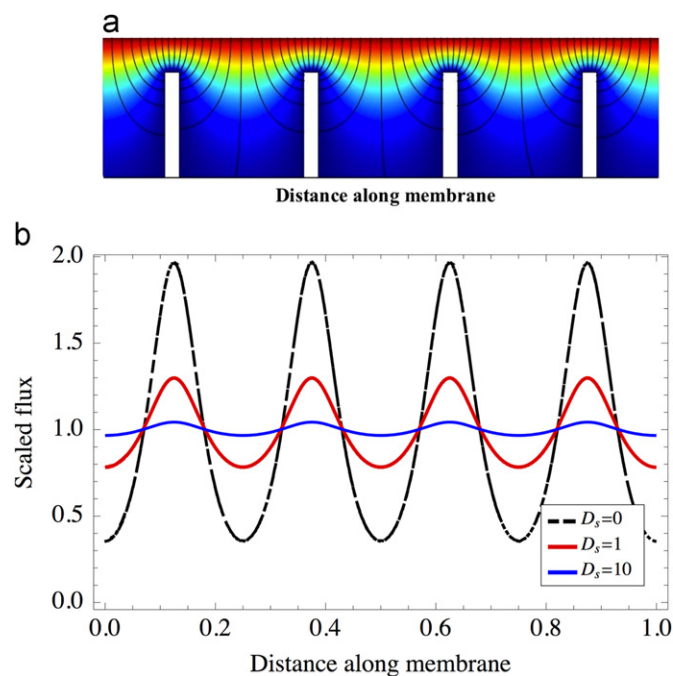

Fig. 8. Flux distribution over the coating film of a composite membrane as affected by the relative diffusion cofficient in the support material, shown for a porosity $\varepsilon = 0.01$, and scaled thickness $H = \delta/R_1 = 5$. (a) Concentration field (note color coding varies from red to blue, denoting high and low concentration, respectively) and diffusive streamlines in a 4-unit representative membrane, for relative diffusivity, $D_S/D_f = 1$. (b) The flux, scaled by the average flux through the film, shown for various values of the relative diffusivity in the support. (For interpretation of the references to color in this figure caption, the reader is referred to the web version of this article.)

Appendix. Calculation of the composite membrane rejection

Employing the solution-diffusion and film theories, the transport through the membrane may be described through the

Table A1
Parameters used for rejection calculations.

	Applied P (bar)	k (m/s)	c_b (g/L)	A (m/Pa s)	B (m/s)
SWRO	60	10^{-5}	32	4×10^{-12}	2×10^{-8}
BWRO	15	10^{-5}	5	6.6×10^{-12}	6×10^{-8}
NF	5	10^{-5}	0.5	2×10^{-11}	9×10^{-7}

following coupled equations:

$$J_W = A(\Delta P - \Delta \pi) \tag{A1}$$

$$J_S = J_W c_p = B(c_m - c_p) \tag{A2}$$

$$\frac{c_m - c_p}{c_b - c_p} \; exp(J_W/k) \tag{A3}$$

where J_W is the water flux, J_S is the salt flux, A and B denote the water and salt permeabilities, respectively, ΔP is the applied hydraulic pressure, k is the mass transfer coefficient and c_m, c_p are the concentrations at the membrane surface and the permeate, respectively. The term $\Delta \pi = 2R_g T(c_m - c_p)$ is the osmotic pressure difference across the membrane (using molar concentrations).

The membrane observed rejection is defined as

$$r_o = 1 - \frac{c_b}{c_p} \tag{A4}$$

where c_b is the concentration in the bulk stream.

In order to calculate the observed rejection, Eqs. (A1)–(A3) were solved iteratively using parameters listed in Table A1, representative of various membrane characteristics. In order to express the dependence of the water and salt permeabilities on the support characteristics, the ratio of the 'real' and 'ideal' permeabilities (Eq. (7)) was multiplied by the A and B values used in the calculation. It should be noted that the theory used herein is not accurate in the case where there is significant coupling between solute and solvent transport. Such effects may be present in NF membranes, and the calculations made herein do not take into account such mechanisms. However, this should not be significant since the presented calculations are mainly useful as illustrations of physical trends, rather than providing any accurate, predictive capacity.

Nomenclature

A	water permeability coefficient
B	salt permeability coefficient
c	concentration
C	scaled concentration
D	diffusion coefficient
H	scaled film thickness, δ/R_1
J	flux
k	mass transfer coefficient
P	permeability
ΔP	applied pressure
r_o	observed rejection
R_1	support membrane pore radius
R_2	periodic cell size
R_g	universal gas constant
T	absolute temperature
X	scaled Cartesian coordinate, x/R_1
Y	scaled Cartesian coordinate, y/R_1
Z	SCALED Cartesian coordinate, z/R_1

Greek letters

δ	thickness of thin film
ε	porosity
π	osmotic pressure

Subscripts

b	bulk
L	long
m	membrane
p	permeate
S	short

References

[1] J.M.S. Henis, M.K. Tripodi, Composite hollow fiber membranes for gas separation: the resistance model approach, J. Membr. Sci. 8 (1981) 233–246.
[2] R.D. Offeman, C.N. Ludvik, A novel method to fabricate high permeance, high selectivity thin-film composite membranes, J. Membr. Sci. 380 (2011) 163–170.
[3] K.P. Lee, T.C. Arnot, D. Mattia, A review of reverse osmosis membrane materials for desalination—development to date and future potential, J. Membr. Sci. 370 (2011) 1–22.
[4] G.R. Guillen, Y. Pan, M. Li, E.M.V. Hoek, Preparation and characterization of membranes formed by nonsolvent induced phase separation: a review, Ind. Eng. Chem. Res. 50 (7) (2011) 3798–3817.
[5] M.T.M. Pendergast, E.M.V. Hoek, A review of water treatment membrane nanotechnologies, Energy Environ. Sci. 4 (2011) 1946–1971.
[6] A.K. Ghosh, B.H. Jeong, X.F. Huang, E.M.V. Hoek, Impacts of reaction and curing conditions on polyamide composite reverse osmosis membrane properties, J. Membr. Sci. 311 (1–2) (2008) 34–45.
[7] B.H. Jeong, E.M.V. Hoek, Y. Yan, A. Subramani, X. Huang, G. Hurwitz, A. Ghosh, A. Jawor, Interfacial polymerization of thin film nanocomposites: a new concept for reverse osmosis membranes, J. Membr. Sci. 294 (2007) 1–7.
[8] M.T.M. Pendergast, A.K. Ghosh, E.M.V. Hoek, Separation performance and interfacial properties of nanocomposite reverse osmosis membranes, Desalination (2011)http://dx.doi.org/10.1016/j.desal.2011.05.005.
[9] A. Tirraferri, N.Y. Yip, W.A. Phillip, J.D. Schiffman, M. Elimelech, Relating performance of thin-film composite forward osmosis membranes to support layer formation and structure, J. Membr. Sci. 367 (2011) 340–352.
[10] A.K. Ghosh, E.M.V. Hoek, Impacts of support membrane structure and chemistry on polyamide–polysulfone interfacial composite membranes, J. Membr. Sci. 336 (2009) 140–148.
[11] H.K Lonsdale, R.L. Riley, C.R. Lyons, D.P. Carosella, Transport incomposite reverse osmosis membranes, in: M. Bier (Ed.), Membrane Processes in Industry and Biomedicine, Plenum Press, New York, 1971, p. 101.
[12] A.M.J. Davis, C.R. Ethier, Transport through materials bounded by porous materials, Chem. Eng. Sci. 48 (9) (1993) 1655–1663.
[13] A.G. Fane, C.J.D. Fell, A.G. Waters, The relationship between membrane surface pore characteristics and flux for ultrafiltration membranes, J. Membr. Sci. 9 (3) (1981) 245–262.
[14] C.R. Ethier, R.D. Kamm, The hydrodynamic resistance of filter cakes, J. Membr. Sci. 43 (1989) 19–30.
[15] J.L. Lopez, S.L. Matson, J. Marchese, J.A. Quinn, Diffusion through composite membranes: a two-dimensional analysis, J. Membr. Sci. 27 (1986) 301–325.
[16] U. Beuschera, C.H. Gooding, The influence of the porous support layer of composite membranes on the separation of binary gas mixtures, J. Membr. Sci. 152 (1999) 99–116.